Journal of Power Sources 209 (2012) 57–64

Contents lists available at SciVerse ScienceDirect

Journal of Power Sources

journal homepage: www.elsevier.com/locate/jpowsour

W-doped $LiW_xNi_{0.5}Mn_{1.5-x}O_4$ cathodes for the improvement of high rate performances in Li ion batteries

S.J. Richard Prabakar, Su Cheol Han, Satendra Pal Singh, Dong Kyu Lee, Kee-Sun Sohn*, Myoungho Pyo*

Department of Printed Electronics Engineering in World Class University (WCU) Program, Sunchon National University, Sunchon, Chonnam 540-742, Republic of Korea

ARTICLE INFO

Article history:
Received 11 January 2012
Received in revised form 13 February 2012
Accepted 15 February 2012
Available online 25 February 2012

Keywords:
Spinel
Cathode
Doping
Tungsten
Lithium ion batteries

ABSTRACT

W-doped $LiW_xNi_{0.5}Mn_{1.5-x}O_4$ ($x = 0.00–0.10$) are synthesized via a sol–gel method, and their electrochemical properties are investigated. During synthesis, W^{4+} is converted to W^{6+}, the amount of which significantly affects the charge–discharge behaviors of $LiW_xNi_{0.5}Mn_{1.5-x}O_4$. When limited to $x \leq 0.005$, W-doping enhances the electrochemical activity of cathodes, leading to a greater discharge capacity and less capacity fading than $LiNi_{0.5}Mn_{1.5}O_4$ at high *C*-rates. This is interesting since lowering the average valence state of Mn ions by incorporating W^{6+} can introduce structural instability, extending a 4 V plateau ($Mn^{3+/4+}$). The reasons for such behavior associated with W-doping are examined by electron microscopy, X-ray photoelectron spectroscopy, X-ray diffraction, and impedance spectroscopy. It is disclosed that the simultaneous increase in Li—O bond length and decrease in transition metal-oxide bond length, while the unit cell volume is maintained almost invariant, provides $LiW_{0.005}Ni_{0.5}Mn_{1.495}O_4$ with optimal high rate performance. When W-doping exceeds $x = 0.01$, 3 factors (intrinsically low electronic conductivity of W^{6+}, the presence of tungsten oxide impurities, and an increase in the inter-metallic distance) aggravates electrochemical performance of $LiW_xNi_{0.5}Mn_{1.5-x}O_4$. The last factor also induces structural instability during repeated cycling because of the expansion of a unit cell volume.

1. Introduction

Among the numerous transition metal oxides applied to the cathode in lithium ion batteries (LIBs), spinel $LiNi_{0.5}Mn_{1.5}O_4$ is considered a promising high-energy material due to its capability to reversibly intercalate lithium ions in a high voltage range (ca. 4.7 V) [1]. The reversible redox process between Ni^{2+} and Ni^{4+}, while the oxidation state of Mn remains unchanged in a 4+ state, results in a high operating voltage, which is possible because the binding energy of the Ni $3de_g$ electrons is at least 0.5 eV higher than that of the Mn $3de_g$ electrons. Despite this unique advantage, however, $LiNi_{0.5}Mn_{1.5}O_4$ remains far from the implementation in commercial LIBs. The main reason is fast-capacity fading particularly at high temperatures, which is also the case with $LiMn_2O_4$ due to electrolyte decomposition and metal ion dissolution [2]. In addition, $LiNi_{0.5}Mn_{1.5}O_4$ can have 2 cubic spinel structures depending on the distribution of Ni and Mn ions (i.e., the $Fd\bar{3}m$ space group with disordered cations or the $P4_332$ space group with 1:3 ordered cations) [3]. The ordered spinel with a $P4_332$ space group experiences a structural transformation during Li extraction, which is another cause for deteriorating capacity during extended cycling [4].

Various strategies have been employed to tackle this point and 2 methods are most frequently employed. The first involves tailoring the particle size into a nanoscale regime to reduce the diffusion length for lithium ions and increase the area of contact with the electrolyte [5–7]. This strategy, however, does not improve the internal electronic conductivity in the crystal and also activates some side reactions on the nanosized material with an organic-based electrolyte, leading to an increase of the polarization effect [8]. The second involves a modification of the intrinsic properties via a partial substitution (doping) of Mn with other metal ions in the crystal structure (or surface coating). Doping can have a direct impact on the structure and stability of $LiNi_{0.5}Mn_{1.5}O_4$ during lithium intercalation/deintercalation. Some transition and non-transition metal elements (Co, Ti, Ru, Fe, Cr, Cu, Mg, Al) have been substituted to stabilize the spinel structure and/or provide facile charge transport [8–12]. In most cases, structural stabilization, minimized polarization, and improved electrical conductivity were obtained via a substitution in low-doping levels. A high concentration of dopants led to detrimental effects in a majority of the cases.

Here, we show that optimized incorporation of W into stoichiometric spinel $LiNi_{0.5}Mn_{1.5}O_4$ can alter the microstructure of the spinel. W-doping at an optimized level increases Li—O bond length

* Corresponding authors. Tel.: +82 61 750 3638; fax: +82 61 750 3608.
E-mail addresses: kssohn@sunchon.ac.kr (K.-S. Sohn), mho@sunchon.ac.kr (M. Pyo).

0378-7753/$ – see front matter © 2012 Elsevier B.V. All rights reserved.
doi:10.1016/j.jpowsour.2012.02.053

and simultaneously decreases Ni—O and Mn—O distances without a substantial change in the unit cell volume. This facilitates Li ion diffusion, leading to greater capacity and better capacity retention than pristine $LiNi_{0.5}Mn_{1.5}O_4$, in particular at a high *C*-rate. To the best of our knowledge, little attention has been paid to W-doping in spinel cathode materials mainly due to the belief that W with a relatively higher oxidation state might induce the reduction of the Mn valence state (Mn^{4+} to Mn^{3+}). Earlier work on W-doping in spinel $LiMn_2O_4$ via solid-state synthesis, however, has shown that with trace level doping the problem with the reduction of Mn valence was insignificant [13]. Moreover, the decrease in the valence state of Mn is not a significant factor in $LiNi_{0.5}Mn_{1.5}O_4$, since a majority of the electrochemical reaction is governed by Ni.

2. Experimental

2.1. Synthesis of $LiW_xNi_{0.5}Mn_{1.5-x}O_4$

Pristine $LiNi_{0.5}Mn_{1.5}O_4$ and W-doped $LiW_xNi_{0.5}Mn_{1.5-x}O_4$ ($x = 0.005, 0.01, 0.025, 0.05, 0.075, 0.10$) were synthesized via a citric acid-assisted sol–gel method. Stoichiometric mixtures of WCl_4,

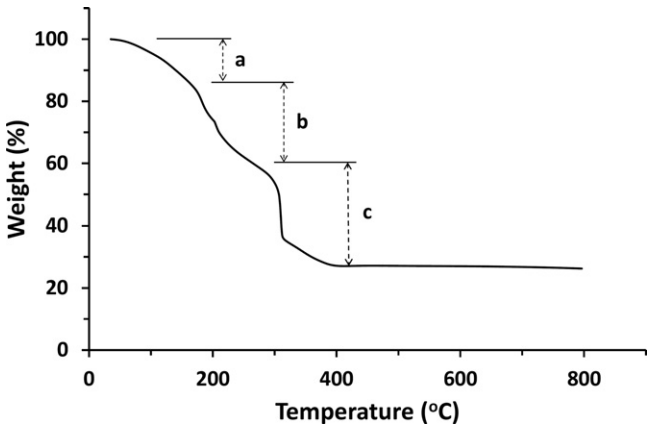

Fig. 1. TGA of $LiW_{0.025}Ni_{0.5}Mn_{1.475}O_4$ precursor at 10 °C min^{-1} in air. Weight losses at each step are due to (a) surface-bound water loss, (b) chemically bonded water loss, and (c) acetate or citrate decomposition.

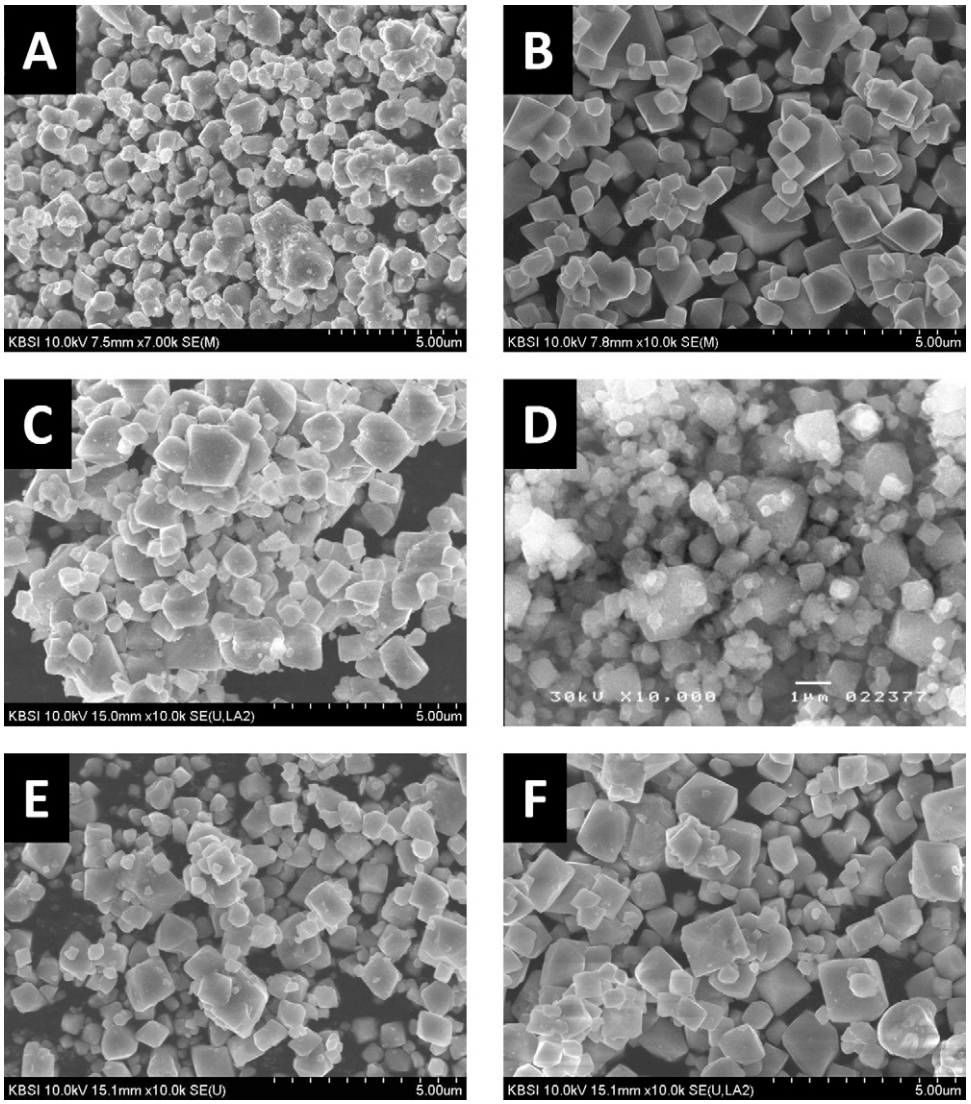

Fig. 2. FESEM images of $LiW_xNi_{0.5}Mn_{1.5-x}O_4$ spinels with various W contents; (A) $x = 0.0$, (B) $x = 0.005$, (C) $x = 0.01$, (D) $x = 0.025$, (E) $x = 0.05$, and (F) $x = 0.1$. (D) image was obtained by JEOL 5310.

Table 1
Summary of structural refinement of $LiNi_{0.5}Mn_{1.5}O_4$ and $LiW_{0.005}Ni_{0.5}Mn_{1.495}O_4$ by a Rietveld method.

Atom	Site	$LiNi_{0.5}Mn_{1.5}O_4$ Fd$\bar{3}$m, a = 8.17169(4) Å, volume = 545.679(4) Å^3, R_p = 21.4, R_{wp} = 9.39, χ^2 = 2.30					$LiW_{0.005}Ni_{0.5}Mn_{1.495}O_4$ Fd$\bar{3}$m, a = 8.17313(2) Å, volume = 545.965(3) Å^3, R_p = 18.8, R_{wp} = 7.71, χ^2 = 1.97				
		x	*y*	*z*	Occupancy	*B*	*x*	*y*	*z*	Occupancy	*B*
Li	8a	0.1250	0.1250	0.1250	0.0417	0.10(9)	0.1250	0.1250	0.1250	0.0417	0.31(8)
Ni	16d	0.5000	0.5000	0.5000	0.0208	0.05(1)	0.5000	0.5000	0.5000	0.0208	0.402(5)
Mn	16d	0.5000	0.5000	0.5000	0.0625	0.05(1)	0.5000	0.5000	0.5000	0.0623	0.403(9)
W	16d	–	–	–			0.5000	0.5000	0.5000	0.0002	0.402(9)
O	32e	0.25822(5)	0.25822(5)	0.25822(5)	0.1667	0.61(1)	0.26122(4)	0.26122(4)	0.26122(4)	0.1667	0.85(1)

Atom	Atom	Inter-atomic distance (Å) for $LiNi_{0.5}Mn_{1.5}O_4$	Inter-atomic distance (Å) for $LiW_{0.005}Ni_{0.5}Mn_{1.495}O_4$
Li	O	1.8856(5)	1.9284(4)
Ni	O	1.9780(5)	1.9559(4)
Mn	O	1.9780(5)	1.9559(4)

$Mn(CH_3COO)_2{\cdot}4H_2O$, $Ni(CH_3COO)_2{\cdot}4H_2O$, and $Li(CH_3COO){\cdot}2H_2O$ (all from Aldrich) were dissolved in triply distilled water in order to obtain clear solutions. Dissolving WCl_4 first and following the sequence mentioned above were important, as any changes resulted in a cloudy sol. Next, the solution was added dropwise to a vigorously stirred aqueous solution of citric acid. The pH of the mixed solution was adjusted to 6.5 by adding an ammonium hydroxide solution. The solution was stirred at 50 °C for 4 h and then heated at 75–80 °C until a transparent gel was obtained. The gel was dried at 80 °C for 12 h in a convection oven, followed by drying in vacuum at 100 °C for 4 h. The resultant gel precursors were ground to a fine powder and decomposed at 450 °C for 2 h in air (a cooling rate of 4 °C min^{-1}). The calcined powder was ground to a fine powder and sintered at 800 °C for 16 h (a cooling rate of 4 °C min^{-1}). Since the presence of W in gels can change the decomposition behavior of the precursor during pre-calcination, thermogravimetric analysis (TGA) was carried out for the $LiW_{0.025}Ni_{0.5}Mn_{1.475}O_4$ gel precursor. Fig. 1 shows the weight loss that occurred in the 3 main steps, which agreed well with previous reports on other manganese oxide spinels [14]. It is evident from the curve that the presence of W did not affect the thermal behavior of gel precursors. There was no change in the TGA profiles as the W content was varied from 0.005 to 0.10.

2.2. Structural characterization and surface analysis

The synthesized oxides were characterized by X-ray diffraction (XRD) using a Rigaku ULTIMA 4 equipped with a Cu K_α radiation at a scan rate of 2° min^{-1}. Morphological and particle size characterizations were carried out using a Hitachi S3500 field emission scanning electron microscope (FESEM) equipped with energy-dispersive X-ray spectroscopy (EDX). The transmission electron microscope (TEM) investigations were performed on a TEM JEOL 2100 instrument with an accelerating voltage of 200 kV. The specimens were prepared by grinding and dispersing a powder in ethanol by ultrasonic treatment for 5 min. The suspensions were dropped on standard holey carbon/Cu grids. The measurements of lattice fringe spacing recorded in high resolution TEM (HRTEM) micrographs were made using a digital image analysis of the reciprocal space parameters. The analysis was conducted using Digital Micrograph software. X-ray photoelectron spectroscopy (XPS) was carried out using a Thermo Fisher (K-Alpha) electron spectrometer with an Al K_α X-ray source (excitation energy = 1486.6 eV). The collected high resolution XPS spectra were analyzed using an XPS peak fitting software program. The energy scale was adjusted with respect to the carbon peak (C1*s*) spectra at 284.5 eV.

2.3. Electrochemical characterization

The electrochemical properties of all cathode electrodes were measured using 2032 coin cells consisting of metallic lithium as an anode and an electrolyte comprised of 1 M $LiPF_6$ in a 1:1 volume fraction of ethylene carbonate (EC)/dimethyl carbonate (DMC). The separator was a Celgard 2400 microporous polypropylene membrane wetted in the electrolyte. The positive electrode, supported onto an aluminum foil, was a mixture containing 90 wt.% of the active $LiW_xNi_{0.5}Mn_{1.5-x}O_4$, 5 wt.% Super P (MTI, USA), and 5 wt.% polyvinylidene fluoride. The cells were assembled in a glove box under an Ar atmosphere (O_2, H_2O < 1 ppm). A galvanostatic charge–discharge cycle test was performed using an automatic WBCS 3000 battery cycler (WonATech) in a potential range of 3.5–4.9 V vs. Li/Li$^+$. The cyclic voltammetry was conducted at a scan rate of 0.2 mV s^{-1}. Electrochemical impedance spectroscopy (EIS) was carried out by applying a 10 mV AC signal over a frequency range of 10^{-1} to 10^5 Hz (PARSTAT 2273).

3. Results and discussion

3.1. SEM studies

The SEM images of the synthesized materials are presented in Fig. 2. Morphological change with W-doping was noticeable. While the pristine $LiNi_{0.5}Mn_{1.5}O_4$ (Fig. 2A) showed rather round-shaped particles and a large proportion of small particles (200–300 nm), the W-doped ones exhibited distinct crystal facets and a decreased ratio of small particles. Note that there were no particles of less than 500 nm in $LiW_{0.1}Ni_{0.5}Mn_{1.4}O_4$ (Fig. 2E). This seems to imply that the presence of small amounts of W heteroatoms might favor crystal growth by releasing microstrains caused by lattice defects. The increased particle size and crystallinity can affect the electrochemical performance of $LiW_xNi_{0.5}Mn_{1.5-x}O_4$ in an opposite direction, which suggests that the fine control of the amounts of W is important. At this point, it is worth mentioning that the EDX analysis showed no residual chloride ions in the samples, which was indicative of no remaining chloride (from the precursor WCl_4) after the sintering process at elevated temperatures.

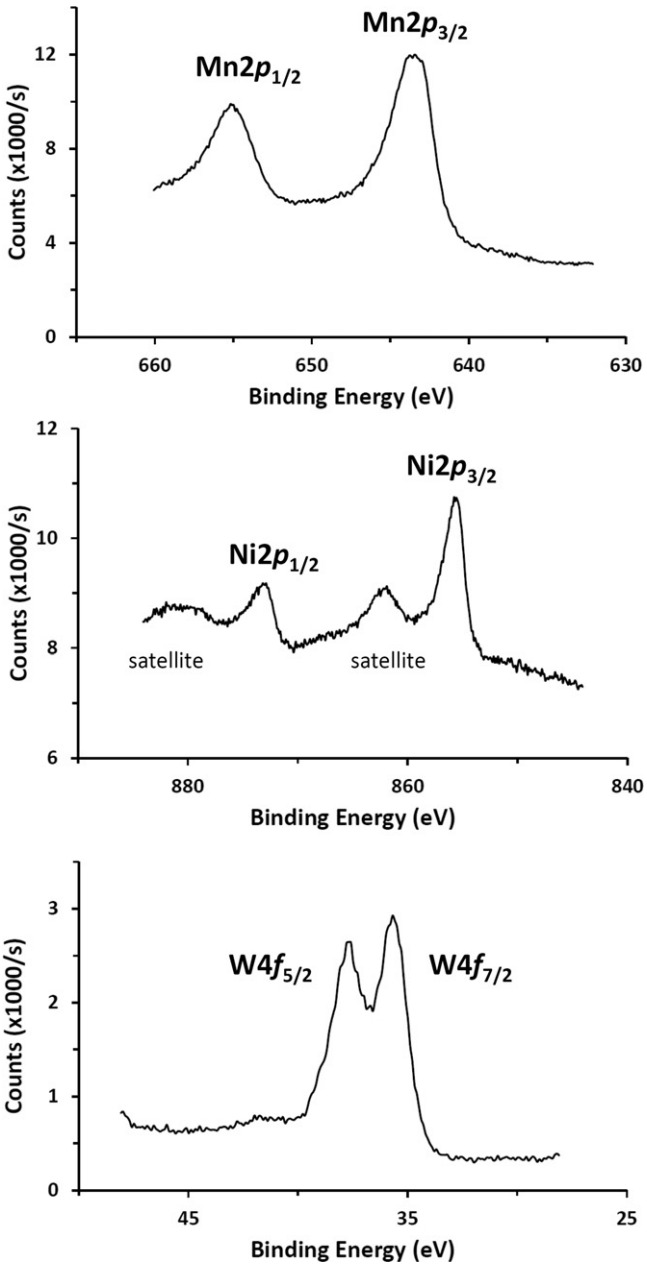

Fig. 3. High resolution X-ray photoelectron spectra of the $LiW_{0.005}Ni_{0.5}Mn_{1.495}O_4$.

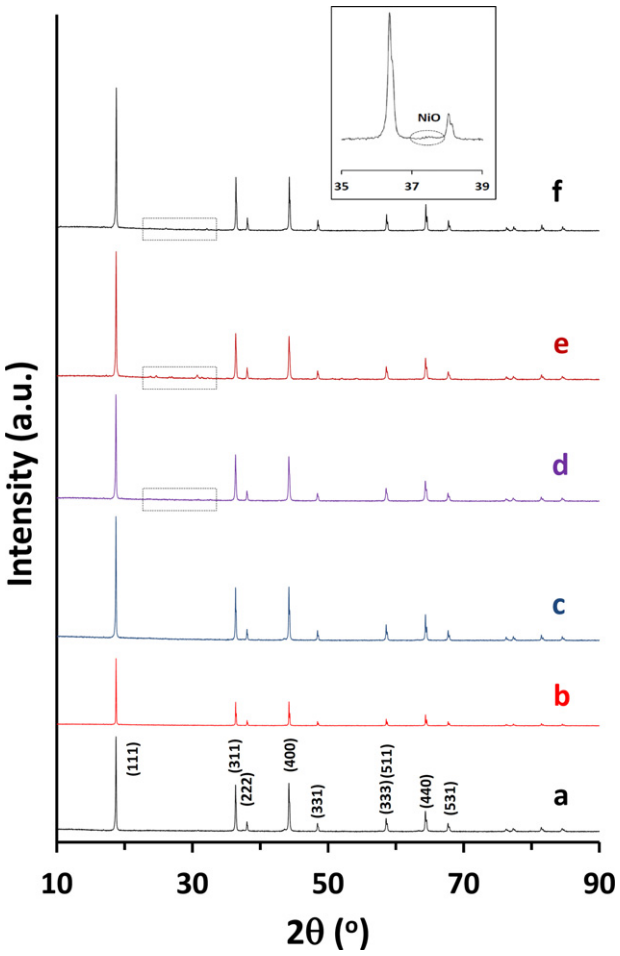

Fig. 4. XRD patterns of (a) $LiNi_{0.5}Mn_{1.5}O_4$, (b) $LiW_{0.005}Ni_{0.5}Mn_{1.495}O_4$, (c) $LiW_{0.01}Ni_{0.5}Mn_{1.49}O_4$, (d) $LiW_{0.025}Ni_{0.5}Mn_{1.475}O_4$, (e) $LiW_{0.05}Ni_{0.5}Mn_{1.45}O_4$, and (f) $LiW_{0.1}Ni_{0.5}Mn_{1.4}O_4$. The dotted squares denote tungsten oxide impurities. Inset shows the most intensive diffraction peak due to the NiO impurity.

3.2. XPS studies

The oxidation state of the transition metal ions were investigated by XPS. Fig. 3 shows the XPS spectra of Mn2*p*, Ni2*p* and W4*f* of $LiW_{0.005}Ni_{0.5}Mn_{1.495}O_4$. The photoelectron peak of C1 *s* was used as a reference (284.5 eV). The characteristic peaks of $Mn2p_{1/2}$ and $Mn2p_{3/2}$ appeared at 655.2 eV and 643.5 eV, respectively. The $Mn2p_{3/2}$ peak was in the vicinity of the value reported for Mn^{4+} [15], which means that the majority of Mn $LiW_{0.005}Ni_{0.5}Mn_{1.495}O_4$ existed in the Mn^{4+} state. The XPS peaks for Ni were located at binding energies of 873.0 eV ($Ni2p_{1/2}$) and 855.5 eV ($Ni2p_{3/2}$) with satellite peaks, supporting the valence state of Ni in 2+ [16]. The observed satellite peak can be ascribed to the multiple splitting of the nickel oxide energy levels by other researchers [17].

The XPS spectra for W4*f* peaks appeared at binding energy of 37.7 eV ($W2f_{5/2}$) and 35.7 eV ($W2f_{7/2}$). The 2 peaks were well separated with no substantial shoulders, indicating that all the W atoms were in the same oxidation state. These values were greater than the binding energy reported for W^{4+} [18], but in good agreement with the reported values of W^{6+} [19]. The oxidation of W^{4+} to W^{6+} during synthesis is explicable, since W is vulnerable to oxidation at very high temperature under air. In the solid-state synthesis of W-doped $LiMn_2O_4$, the metallic W powder was completely oxidized, making no significant difference from WO_3 [13].

3.3. Structure characterization

The XRD patterns of pristine $LiNi_{0.5}Mn_{1.5}O_4$ were compared with those of the W-doped $LiW_xNi_{0.5}Mn_{1.5-x}O_4$ ($x = 0.005$, 0.01, 0.025, 0.05, and 0.1). Fig. 4 shows that all XRD patterns could be indexed in the $Fd\bar{3}m$ space group, corresponding to a cubic spinel. In this phase, while the Ni^{2+} and the Mn^{4+} ions randomly occupy the octahedral 16*d* sites, the Li^+ ions occupy the tetrahedral 8*a* sites. Although not obvious, all samples showed weak Bragg peaks corresponding to an impurity of NiO, which is common for spinels sintered at high temperatures [20]. The XRD data also revealed the presence of a trace level of another impurity when $x \geq 0.01$ (dotted squares in Fig. 4d–f). This can be ascribed to the diffraction from various crystal forms of tungsten oxide.

For a better understanding of the effect of W-doping on cell parameters and atomic arrangements, Rietveld refinement was performed using a Fullprof package [21]. In the refinements, a pseudo-Voigt function and a linear interpolation between the set

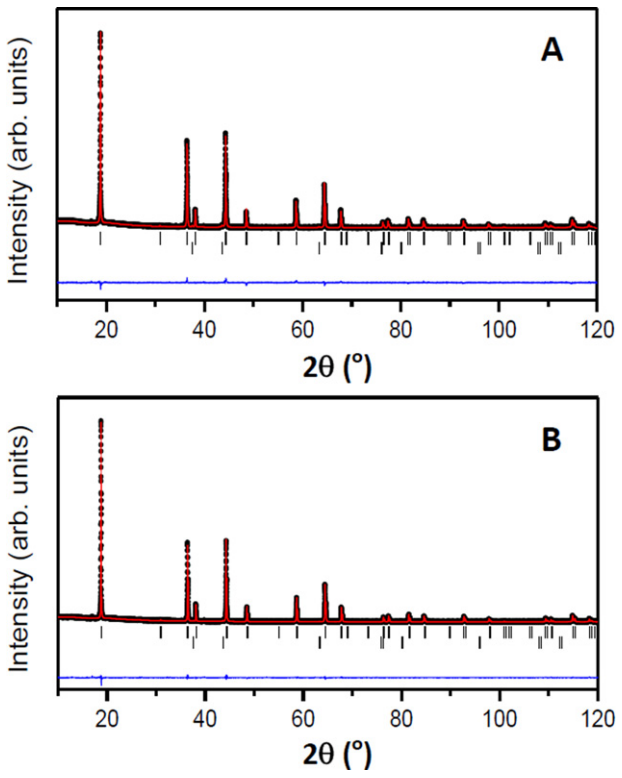

Fig. 5. Observed (dot), calculated (red line), and difference (blue line) profiles obtained after full pattern Rietveld refinements using powder X-ray diffraction data in the 2θ range of 10° to 120° for (A) $LiNi_{0.5}Mn_{1.5}O_4$ and (B) $LiW_{0.005}Ni_{0.5}Mn_{1.495}O_4$, using cubic structure in a $Fd\bar{3}m$ space group. The tick marks above the difference plot show the position of the Bragg peaks. A small fraction of NiO (impurity phase) was fitted using cubic structure in the $Fm\bar{3}m$ space group. (For interpretation of the references to color in this figure legend, the reader is referred to the web version of this article.)

background points with refinable heights were used to define the profile shape and the background, respectively. Except for the occupancy parameters of the ions, which were fixed at the nominal composition, all other parameters such as scale factor, zero correction, background, half-width parameters, the mixing parameters, lattice parameters, positional coordinates, and thermal parameters were varied in the course of refinement. Fig. 5 depicts the Rietveld fit for the pristine $LiNi_{0.5}Mn_{1.5}O_4$ and $LiW_{0.005}Ni_{0.5}Mn_{1.495}O_4$ using a cubic spinel in the $Fd\bar{3}m$ space group. The refined parameters are summarized in Table 1. Since a small amount of NiO was detected as an impurity phase, the Rietveld refinement was carried out including the NiO phase with a cubic structure in the $Fm\bar{3}m$ space group.

It is evident from Fig. 5 that a very good fit between the observed and calculated data were obtained with reasonably good agreement factors. The value of the agreement factors for the pristine $LiNi_{0.5}Mn_{1.5}O_4$ and $LiW_{0.005}Ni_{0.5}Mn_{1.495}O_4$ was $R_p = 21.44$ and 18.8, $R_{wp} = 9.39$ and 7.71, $R_e = 6.19$ and 5.48, and $\chi^2 = 2.30$ and 1.97, respectively. It is worth mentioning here that we observed no superlattice reflection in the XRD patterns, implying that the cation ordering giving a space group of $P4_332$ was not the case here. This was further confirmed using HRTEM studies, as discussed below. A refinement result also indicated that the change in unit cell dimensions was negligible for W-doping of $x = 0.005$. Note that the unit cell volume was increased from 545.679(4) Å^3 to 545.965(3) Å^3. A rather surprising difference came from the variation in Li—O inter-atomic distance. While the Li—O distance was significantly increased upon W-doping (1.8856(5) Å vs. 1.9284(5) Å), the volume of NiO_6 and MnO_6 octahedrons shrank to compensate for the unit cell expansion. The increase in volume of the LiO_4 tetrahedron was interesting because it suggested the possible effectiveness of W-doping with respect to fast electrochemical kinetics. However, this behavior was not observed for $LiW_{0.01}Ni_{0.5}Mn_{1.49}$ as the unit cell volume suddenly increased to 553.950(3) Å^3, suggesting that the optimal concentration of W in $LiW_xNi_{0.5}Mn_{1.5-x}O_4$ by sol–gel synthesis would be $x = 0.005$. Therefore, we concentrated more on $LiW_{0.005}Ni_{0.5}Mn_{1.495}O_4$ for further investigations. Note that, due to the presence of tungsten oxide impurities in the samples doped with W higher than $x = 0.01$, more detailed discussion from the Rietveld refinement result of $LiW_xNi_{0.5}Mn_{1.5-x}O_4$ ($x > 0.01$) would be pointless.

The crystalline structure of the $LiW_{0.005}Ni_{0.5}Mn_{1.495}O_4$ sample was further examined by HRTEM. As shown in Fig. 6, $LiW_{0.005}Ni_{0.5}Mn_{1.495}O_4$ consisted of a well-crystallized hexagonal packing pattern. Fig. 6 also shows (1 1 1) and (0 0 2) lattice fringes with interplanar spacing of ca. 0.48 nm and 0.41 nm, respectively. These values were in good agreement with those obtained from the XRD analysis. For example, the (1 1 1) interplanar spacing obtained from XRD was 0.47 nm for both pristine $LiNi_{0.5}Mn_{1.5}O_4$ and $LiW_{0.005}Ni_{0.5}Mn_{1.495}O_4$ samples. Due to the similar scattering factors for Ni and Mn, the standard XRD technique could not suitably distinguish between the 2 cubic modifications ($Fd\bar{3}m$ and $P4_332$ space groups) of $LiNi_{0.5}Mn_{1.5}O_4$. However, the selected area

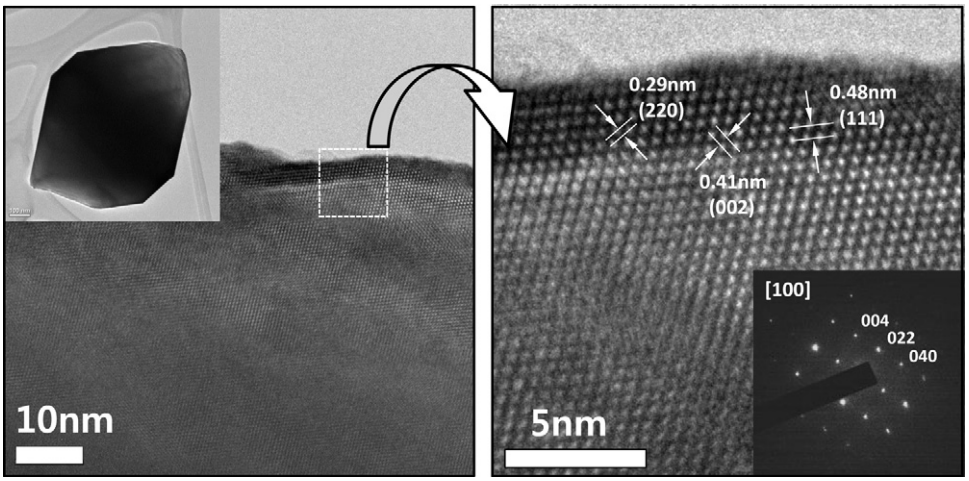

Fig. 6. HRTEM images showing a single $LiW_{0.005}Ni_{0.5}Mn_{1.495}O_4$ particle (left). Magnified view of a dotted square in the image at right. The inset shows a selected area electron diffraction pattern taken along the [1 0 0] orientation.

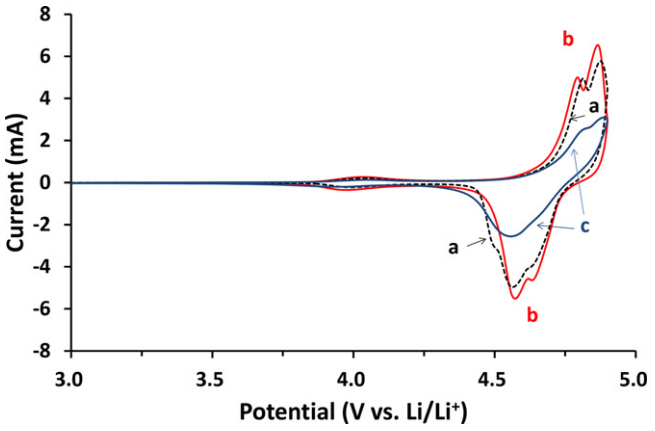

Fig. 7. CVs of (a) $LiNi_{0.5}Mn_{1.5}O_4$, (b) $LiW_{0.005}Ni_{0.5}Mn_{1.495}O_4$, and (c) $LiW_{0.01}Ni_{0.5}Mn_{1.49}O_4$ measured at a scan rate of 0.2 mV s^{-1}.

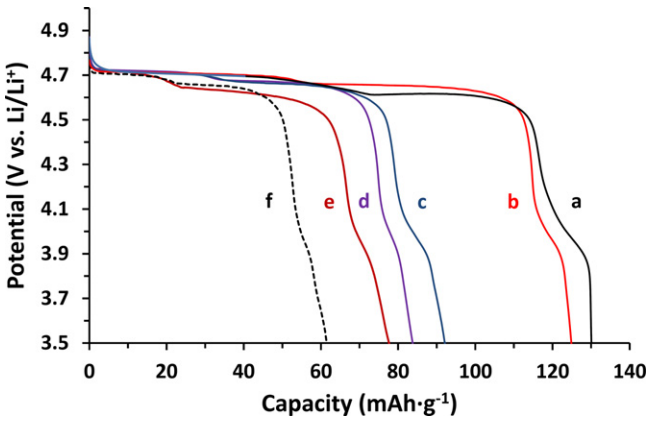

Fig. 8. Discharge curves for the first cycle at 0.1 C; (a) $LiNi_{0.5}Mn_{1.5}O_4$, (b) $LiW_{0.005}Ni_{0.5}Mn_{1.495}O_4$, (c) $LiW_{0.01}Ni_{0.5}Mn_{1.49}O_4$, (d) $LiW_{0.025}Ni_{0.5}Mn_{1.475}O_4$, (e) $LiW_{0.05}Ni_{0.5}Mn_{1.45}O_4$, and (f) $LiW_{0.1}Ni_{0.5}Mn_{1.4}O_4$.

electron diffraction (SAED) pattern taken at the [1 0 0] zone axis showed the absence of the superlattice spots, clearly indicating a cation disordering in $LiW_{0.005}Ni_{0.5}Mn_{1.495}O_4$ and a space group of $Fd\bar{3}m$ [22]. All diffraction spots could be indexed using the $Fd\bar{3}m$ space group.

3.4. Electrochemical characterization and performance

Based on the structure characterizations mentioned above, a cyclic voltammogram (CV) of $LiW_{0.005}Ni_{0.5}Mn_{1.495}O_4$ was compared with cyclic voltammogram (CVs) of pristine $LiNi_{0.5}Mn_{1.5}O_4$ and $LiW_{0.01}Ni_{0.5}Mn_{1.49}O_4$ (Fig. 7). The CVs in general show one small redox pair at ca. 4.0 V corresponding to a $Mn^{3+/4+}$ couple (Mn^{3+} resulting from the non-stoichiometry) and the other 2 dominant pairs at ca. 4.7 V resulting from a redox process of $Ni^{2+/4+}$. The latter may be due to the progressive electron transfer between Ni^{2+} and Ni^{4+} through Ni^{3+} [23]. The $LiW_{0.005}Ni_{0.5}Mn_{1.495}O_4$ had a very similar peak shape when compared to pristine $LiNi_{0.5}Mn_{1.5}O_4$, but with slightly sharper peaks and a narrower peak separation (ΔE_p). On the contrary, $LiW_{0.01}Ni_{0.5}Mn_{1.49}O_4$ demonstrated considerably broad redox peaks. In addition, the ΔE_p value became larger with a substantial shift of the cathodic peak to negative potentials. On the other hand, the peaks at the 4 V region seemed unaffected in the samples analyzed, meaning that the non-stoichiometry was not severely influenced by the W substitution within $x \leq 0.01$.

The initial discharge curves of the pristine $LiNi_{0.5}Mn_{1.5}O_4$ and $LiW_xNi_{0.5}Mn_{1.5-x}O_4$ ($x = 0.005$, 0.01, 0.025, 0.05, and 0.1) at 0.1 C were also compared in Fig. 8. The initial discharge capacities of pristine $LiNi_{0.5}Mn_{1.5}O_4$ and $LiW_xNi_{0.5}Mn_{1.5-x}O_4$ were 130.1 mAh g^{-1} and 124.9 ($x = 0.005$), 92.1 ($x = 0.01$), 83.8 ($x = 0.025$), 77.6 ($x = 0.05$), and 51.5 ($x = 0.1$) mAh g^{-1}. While a slight decrease in capacity (5.2 mAh g^{-1}) for $LiW_{0.005}Ni_{0.5}Mn_{1.495}O_4$ was observed, initial discharge capacities of $LiW_xNi_{0.5}Mn_{1.5-x}O_4$ ($x \geq 0.01$) were decreased drastically with an increase in the content of W. The plateau potentials were also affected by the W content. For $LiW_{0.05}Ni_{0.5}Mn_{1.45}O_4$ and $LiW_{0.1}Ni_{0.5}Mn_{1.4}O_4$ (Fig. 8e and f), the polarization led to a lowering of the discharge potential by ca. 0.1 V when compared with $LiNi_{0.5}Mn_{1.5}O_4$ and $LiW_{0.005}Ni_{0.5}Mn_{1.495}O_4$.

Fig. 8 also shows that the small plateau occurring at 4.0 V was decreased by W-doping. This was unexpected since the increased replacement of tetravalent Mn by hexavalent W should result in an increase of the 4.0 V-active Mn^{3+} amounts (even though a fraction of Mn content is reduced by substitution). However, the reverse behavior was observed showing a diminution of the 4.0 V plateau. This was a clear indication that, when the W content is high, a substantial fraction of W^{6+} exists as oxide impurities rather than being involved in the crystalline structure.

The effect of *C*-rates on the discharge capacity with variation of the W content was investigated. Fig. 9 shows that the capacity decreased gradually with an increase as high as 1.0 C in the current density for all samples. As expected from Fig. 8, the capacities of W-doped samples were less than that of $LiNi_{0.5}Mn_{1.5}O_4$ and decreased with W in these *C*-rate regimes. When the *C*-rate was further increased to 3.0 C, this trend no longer held. While the capacity dropped drastically for all samples, only $LiW_{0.005}Ni_{0.5}Mn_{1.495}O_4$ exhibited a slight decrease in capacity, resulting in the greatest capacity among the samples examined.

The best performance of $LiW_{0.005}Ni_{0.5}Mn_{1.495}O_4$ at high *C*-rates and the negative effect of W-doping for $x \geq 0.10$ can be explained as follows. First, SEM studies (Fig. 2) revealed that the particle size and crystallinity were increased with W-doping. These 2 parameters affect the Li ion diffusion in an opposite direction. The effect of higher crystallinity can be offset by the increase in diffusion length with W-doping. Therefore, the influence of these parameters on electrochemical performance is likely minimal at best. Second, relatively heavy-doped $LiW_xNi_{0.5}Mn_{1.5-x}O_4$ ($x \geq 0.01$) can experience the retardation of electron transfer. The flux of Li ions in the crystal lattice is followed by an electron exchange at the redox active sites ($Ni^{2+/4+}$) and by final transfer of the electron via a hopping mechanism [24]. This means that the electron transfer pathway should involve Ni—O—W—O, since the first coordination shell of Ni is oxygen, followed by Mn or W. For this kind of an electron transfer to proceed, the dopant W ions should be able to accept

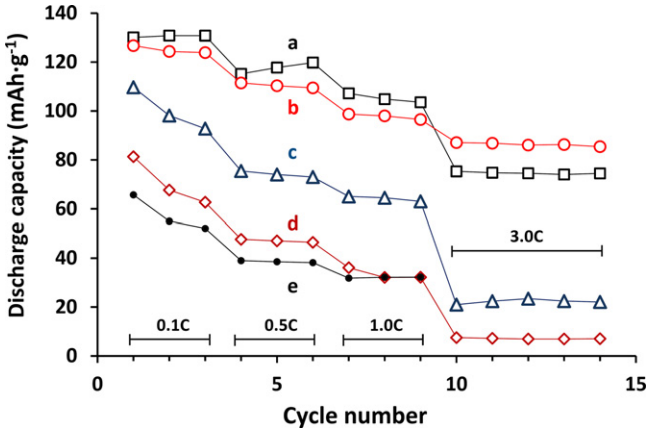

Fig. 9. Change of discharge capacity with *C*-rates; (a) $LiNi_{0.5}Mn_{1.5}O_4$, (b) $LiW_{0.005}Ni_{0.5}Mn_{1.495}O_4$, (c) $LiW_{0.01}Ni_{0.5}Mn_{1.49}O_4$, (d) $LiW_{0.05}Ni_{0.5}Mn_{1.45}O_4$, and (e) $LiW_{0.1}Ni_{0.5}Mn_{1.4}O_4$.

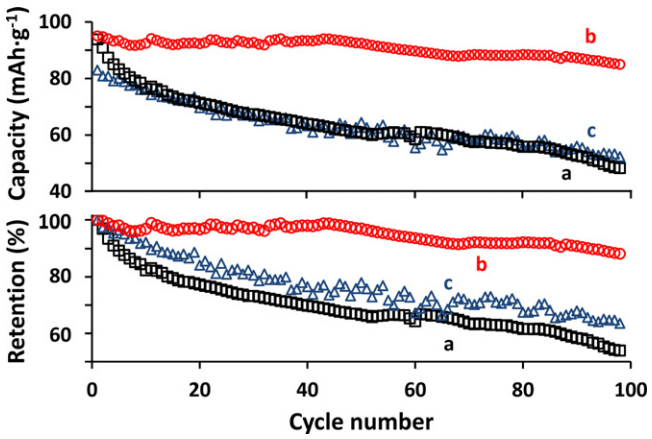

Fig. 10. Evolution of discharge capacities of (a) $LiNi_{0.5}Mn_{1.5}O_4$, (b) $LiW_{0.005}Ni_{0.5}Mn_{1.495}O_4$, and (c) $LiW_{0.01}Ni_{0.5}Mn_{1.49}O_4$ at 3.0 C for 98 cycles. Change of specific capacities (top) and normalized capacity retention (bottom).

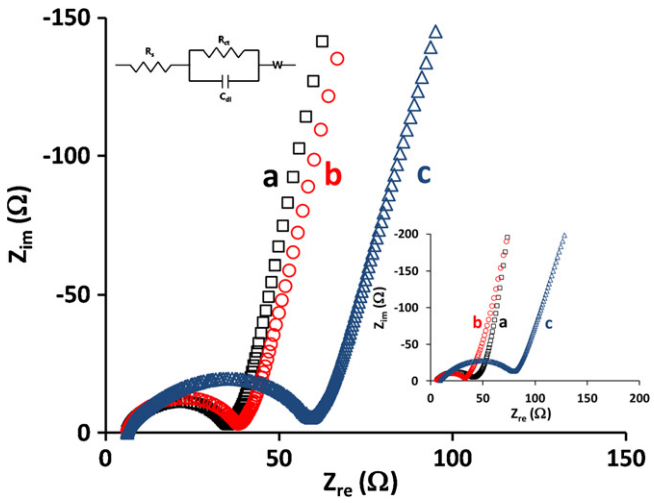

Fig. 11. Electrochemical impedance spectra of (a) $LiNi_{0.5}Mn_{1.5}O_4$, (b) $LiW_{0.005}Ni_{0.5}Mn_{1.495}O_4$, and (c) $LiW_{0.01}Ni_{0.5}Mn_{1.49}O_4$. The inset shows the change of impedance spectra after a single charge–discharge cycle at 0.1 C.

a local variation of the valence. However, W^{6+} exhibiting a full shell configuration ($4f^{14}$) was unable to accept a local variation of the valence, thereby impeding the electron transfer. In addition, the formation of tungsten oxide impurities for samples with $x \geq 0.01$ also developed a highly resistive insulating surface layer [1,25]. Finally, although W-doping aggravated the electrochemical performance, that was not the case for $LiW_{0.005}Ni_{0.5}Mn_{1.495}O_4$. An increase in the Li—O inter-atomic distance without expanding the cell volume (Rietveld refinement in Fig. 5 and Table 1) expedited the Li intercalation/deintercalation and exhibited a relatively weak *C*-rate dependence of discharge capacity.

Since the change in inter-atomic distances for $LiW_{0.005}Ni_{0.5}Mn_{1.495}O_4$ (Fig. 5 and Table 1) can affect the structural integrity during repeated Li intercalation/deintercalation, the capacity retention was examined and compared with $LiNi_{0.5}Mn_{1.5}O_4$ and $LiW_{0.01}Ni_{0.5}Mn_{1.49}O_4$. Fig. 10 shows the capacity changes in (a) pristine $LiNi_{0.5}Mn_{1.5}O_4$, (b) $LiW_{0.005}Ni_{0.5}Mn_{1.495}O_4$, and (c) $LiW_{0.01}Ni_{0.5}Mn_{1.49}O_4$ for 98 cycles at 3.0 C. While the initial capacity of $LiNi_{0.5}Mn_{1.5}O_4$ and $LiW_{0.005}Ni_{0.5}Mn_{1.495}O_4$ were similar to one another, $LiW_{0.01}Ni_{0.5}Mn_{1.49}O_4$ showed a slightly lower initial capacity, which corresponded to the results shown in Fig. 9. (In Fig. 9, the capacity of $LiNi_{0.5}Mn_{1.5}O_4$ at 3.0 C was lower than that of $LiW_{0.005}Ni_{0.5}Mn_{1.495}O_4$ because of cycling history.) The capacity of $LiNi_{0.5}Mn_{1.5}O_4$, however, faded quickly and retained only 51.4% of the initial capacity after 98 cycles. $LiW_{0.01}Ni_{0.5}Mn_{1.49}O_4$ also exhibited similar capacity fading behaviors, reaching the final capacity of 52.3 mAh g^{-1} (63.0% capacity retention). However, the decrease in the capacity for $LiW_{0.005}Ni_{0.5}Mn_{1.495}O_4$ was substantially alleviated, which resulted in a capacity retention of 89.4%. (The initial capacity of 95.1 mAh g^{-1} decreased to 85.0 mAh g^{-1} after 98 cycles.) This outstanding stability of $LiW_{0.005}Ni_{0.5}Mn_{1.495}O_4$ appears to result from the increase in the Mn—O and Ni—O bond energy, while the expansion of the LiO_4 tetrahedron contributes to the fast Li ion diffusion.

EIS measurements were carried out after storing the cells at room temperature for 1 h. The Nyquist plots were recorded from 1 MHz to 0.1 Hz for (a) $LiNi_{0.5}Mn_{1.5}O_4$, (b) $LiW_{0.005}Ni_{0.5}Mn_{1.495}O_4$, and (c) $LiW_{0.01}Ni_{0.5}Mn_{1.49}O_4$ before (Fig. 11) and after (Fig. 11, inset) a single charge–discharge cycle at 0.1 C. All Nyquist plots consisted of one semicircle and a Warburg impedance corresponding to the charge transfer at the electrolyte/electrode interface (R_{ct} and C_{dl}) and the Li diffusion in the crystal lattice, respectively [26,27]. The electrolyte resistance (R_s) remained almost constant, which was expected since the variation of an electrolyte concentration was not so large as to affect the electrolyte conductivity. The resistance and capacitance due to a solid-electrolyte interface (SEI) layer were not discernible and appeared to merge into the semi-circle from a charge transfer. Fig. 11 shows that although the semicircle was the smallest for the pristine $LiNi_{0.5}Mn_{1.5}O_4$ (R_{ct} = 29.1 Ω), $LiW_{0.005}Ni_{0.5}Mn_{1.495}O_4$ also showed a comparable charge transfer resistance (R_{ct} = 31.9 Ω). $LiW_{0.01}Ni_{0.5}Mn_{1.49}O_4$, however, exhibited ca. twice the resistance of $LiNi_{0.5}Mn_{1.5}O_4$ and $LiW_{0.005}Ni_{0.5}Mn_{1.495}O_4$ (R_{ct} = 52.9 Ω). This difference in EIS spectra agreed well with the aforementioned analysis. The unit cell expansion (i.e., increase in bond distance between transition metal ions) along with the presence of oxide impurities and excessive incorporation of W^{6+} beyond a critical W-doping led to a significant increase in R_{ct} for $LiW_{0.01}Ni_{0.5}Mn_{1.49}O_4$. After a single charge–discharge cycle at 0.1 C, the R_{ct} of $LiW_{0.01}Ni_{0.5}Mn_{1.49}O_4$ was further increased to 70.0 Ω, which was indicative of a structural instability and SEI layer formation. The R_{ct} of $LiNi_{0.5}Mn_{1.5}O_4$ was also slightly increased to 34.5 Ω due to a surface SEI film, but $LiW_{0.005}Ni_{0.5}Mn_{1.495}O_4$ showed a lowered R_{ct} (26.9 Ω) after a charge–discharge cycle. The reason for the R_{ct} decrease in the latter is not clear at this point, but is likely related to the enhanced structural integrity.

4. Conclusion

W-doped $LiW_xNi_{0.5}Mn_{1.5-x}O_4$ (x = 0.000–0.1) synthesized by a sol–gel method are investigated. With the exception of lightly doped $LiW_{0.005}Ni_{0.5}Mn_{1.495}O_4$, the incorporation of W^{6+}, evidenced by XPS, lowers specific capacities and aggravated capacity retention. $LiW_{0.005}Ni_{0.5}Mn_{1.495}O_4$ shows an initial capacity value that is slightly higher than $LiNi_{0.5}Mn_{1.5}O_4$ at 3.0 C, but a remarkably greater capacity retention after ca. 100 charge–discharge cycles. While the capacity is reduced to ca. a half for $LiNi_{0.5}Mn_{1.5}O_4$, ca. 90% of initial capacity is retained in $LiW_{0.005}Ni_{0.5}Mn_{1.495}O_4$.

Although the incorporation of W^{6+} increases the crystallinity, it also produces large-sized particles, meaning that the influence of these two effects on Li ion diffusion might be canceled. The best performance of $LiW_{0.005}Ni_{0.5}Mn_{1.495}O_4$ at high *C*-rates results from the change of inter-atomic distances. The increase in Li—O length makes Li intercalation/deintercalation easier, minimizing the capacity decrease at high *C*-rates. A structural stability as well as a facile electron transfer was provided by the shrinkage of transition metal-oxide octahedrons. When the amount of W is further increased ($x \geq 0.01$ in $LiW_xNi_{0.5}Mn_{1.5-x}O_4$), the

intrinsically low conductivity of W^{6+} and the presence of impurities hampers electron transfer and decreases discharge capacities. The structural stability is also aggravated in these cases (severe capacity fading), because W-doping abruptly increases the unit cell volume.

Acknowledgments

This research was supported by the WCU (World Class University) program through the Korea Science and Engineering Foundation funded by the Ministry of Education, Science and Technology (R31-10022).

References

[1] Q. Zhong, A. Bonakdarpour, M. Zhang, Y. Gao, J.R. Dahn, J. Electrochem. Soc. 144 (1997) 205–213.
[2] Y. Fan, J. Wang, Z. Tang, W. Hea, J. Zhang, Electrochim. Acta 52 (2007) 3870–3875.
[3] K. Ariyoshi, Y. Iwakoshi, N. Nakayama, T. Ohzuku, J. Electrochem. Soc. 151 (2004) A296–A303.
[4] J.H. Kim, S.T. Myung, C.S. Yoon, S.G. Kang, Y.K. Sun, Chem. Mater. 16 (2004) 906–914.
[5] J.C. Arrebola, A. Caballero, M. Cruz, L. Hernan, J. Morales, E.R. Castellon, Adv. Funct. Mater. 16 (2006) 1904–1912.
[6] H.Y. Xu, S. Xie, N. Ding, B.L. Liu, Y. Shang, C.H. Chen, Electrochim. Acta 51 (2006) 4352–4357.
[7] S.T. Myung, S. Komaba, N. Kumagai, H. Yashiro, H.T. Chung, T.H. Cho, Electrochim. Acta 47 (2002) 2543–2549.
[8] C.V. Rao, A.L.M. Reddy, Y. Ishikawa, P.M. Ajayan, Appl. Mater. Interfaces 3 (2011) 2966–2972.
[9] M.-L.-P. Le, P. Strobela, F. Alloinb, T. Pagnier, Electrochim. Acta 56 (2010) 592–599.
[10] J. Liu, A. Manthiram, J. Phys. Chem. C 113 (2009) 15073–15079.
[11] M. Aklalouch, J.M. Amarilla, R.M. Rojas, I. Saadoune, J.M. Rojo, J. Power Sources 185 (2008) 501–511.
[12] G.T.-K. Fey, C.-Z. Lu, T.P. Kumar, J. Power Sources 115 (2003) 332–345.
[13] A. Eftekhari, A.B. Moghaddam, B. Yazdani, F. Moztarzadeh, Electrochim. Acta 52 (2006) 1491–1498.
[14] T. Yi, X. Hu, K. Gao, J. Power Sources 162 (2006) 636–643.
[15] S.H. Kang, J. Kim, M.E. Stoll, D. Abraham, Y.K. Sun, K. Amine, J. Power Sources 112 (2002) 41–48.
[16] S. Rajakumar, R. Thirunakaran, A. Sivashanmugam, J.-I. Yamaki, S. Gopukumar, J. Electrochem. Soc. 156 (2009) A246–A252.
[17] S. Gopukumar, K.Y. Chung, K.B. Kim, Electrochim. Acta 49 (2004) 803–810.
[18] C.S. Blackman, C. Piccirillo, R. Binions, I.P. Parkin, Thin Solid Films 517 (2009) 4565–4570.
[19] H. Qi, C.Y. Wang, J. Liu, Adv. Mater. 15 (2003) 411–414.
[20] M.-C. Yang, B. Xu, J.-H. Cheng, C.-J. Pan, B.-J. Hwang, Y.S. Meng, Chem. Mater. 23 (2011) 2832–2841.
[21] J. Rodriguez-Carvajal, FULLPROF, Laboratory Leon Brillouin CEA-CNRSCEA/Saclay, 91191 Gif sur Yvette Cedex, France, Version May 2010.
[22] S. Ivanova, E. Zhecheva, R. Stoyanova, D. Nihtianova, S. Wegner, P. Tzvetkova, S. Simova, J. Phys. Chem. C 115 (2011) 25170–25182.
[23] K.A. Striebel, A. Rougier, C.R. Horne, R.P. Reade, E.J. Cairns, J. Electrochem. Soc. 146 (1999) 4339.
[24] M.-L.-P. Le, P. Strobel, F. Alloin, T. Pagnier, Electrochim. Acta 56 (2010) 592–599.
[25] J. Liu, A. Manthiram, Chem. Mater. 21 (2009) 1695–1707.
[26] D. Aurbach, M. Levi, E. Levi, H. Teller, B. Markovsky, G. Salitra, U. Heider, J. Electrochem. Soc. 145 (1998) 3024–3034.
[27] M. Levi, G. Salitra, B. Markovsky, H. Teller, D. Aurbach, L. Heider, J. Electrochem. Soc. 146 (1999) 1279–1289.